

Precise inter-polar phasing of abrupt climate change during the last ice age

WAIS Divide Project Members*

The last glacial period exhibited abrupt Dansgaard–Oeschger climatic oscillations, evidence of which is preserved in a variety of Northern Hemisphere palaeoclimate archives¹. Ice cores show that Antarctica cooled during the warm phases of the Greenland Dansgaard–Oeschger cycle and vice versa^{2,3}, suggesting an inter-hemispheric redistribution of heat through a mechanism called the bipolar seesaw^{4–6}. Variations in the Atlantic meridional overturning circulation (AMOC) strength are thought to have been important, but much uncertainty remains regarding the dynamics and trigger of these abrupt events^{7–9}. Key information is contained in the relative phasing of hemispheric climate variations, yet the large, poorly constrained difference between gas age and ice age and the relatively low resolution of methane records from Antarctic ice cores have so far precluded methane-based synchronization at the required sub-centennial precision^{3,3,10}. Here we use a recently drilled high-accumulation Antarctic ice core to show that, on average, abrupt Greenland warming leads the corresponding Antarctic cooling onset by 218 ± 92 years (2σ) for Dansgaard–Oeschger events, including the Bølling event; Greenland cooling leads the corresponding onset of Antarctic warming by 208 ± 96 years. Our results demonstrate a north-to-south directionality of the abrupt climatic signal, which is propagated to the Southern Hemisphere high latitudes by oceanic rather than atmospheric processes. The similar inter-polar phasing of warming and cooling transitions suggests that the transfer time of the climatic signal is independent of the AMOC background state. Our findings confirm a central role for ocean circulation in the bipolar seesaw and provide clear criteria for assessing hypotheses and model simulations of Dansgaard–Oeschger dynamics.

Net heat transport by the Atlantic branch of the global ocean overturning circulation is northwards at all latitudes, resulting in a heat flux from the Southern Hemisphere (SH) to the Northern Hemisphere (NH)⁴. Variations in this flux act to redistribute heat between the hemispheres, a mechanism commonly invoked to explain abrupt sub-orbital climatic variability and the asynchronous coupling of Greenland and Antarctic temperature variations on these timescales^{2,6}. Millennial-scale AMOC variability is corroborated by North Atlantic proxies for deep-water ventilation and provenance that suggest decreased North Atlantic deep water production and the intrusion of southern-sourced water masses during stadial (that is, North Atlantic cold) periods^{11,12}. The oceanic instabilities are accompanied by shifting atmospheric transport patterns. Proxy data and climate models consistently indicate northward and southward migrations of the intertropical convergence zone in response to abrupt NH warming and cooling, respectively^{13,14}. Abrupt NH events may also induce changes in the strength and position of the SH mid-latitude westerlies. Strengthened and/or southward-shifted westerlies during NH stadials have the potential to warm the Southern Ocean and Antarctica by enhancing the wind-driven upwelling of relatively warm circumpolar deep waters, providing a direct atmospheric pathway for the bipolar seesaw to operate¹⁵. Climate model simulations further suggest that atmospheric readjustment in response to decreased North Atlantic

deep water formation can induce inhomogeneous temperature changes over the Antarctic continent^{16,17}, possibly by means of wind-driven changes in sea-ice distribution⁸.

Atmospheric teleconnections operate on seasonal to decadal timescales because of the fast response time of the atmosphere^{8,18,19}. By contrast, oceanic teleconnections can operate on a wide range of timescales from decadal to multi-millennial, depending on the processes and ocean basins involved^{19–21}. Climatic signals can be rapidly propagated from the North Atlantic to the South Atlantic via Kelvin waves⁵, but models suggest a more gradual (centennial timescale) propagation from the South Atlantic to the SH high latitudes as a result of the absence of a zonal topographic boundary at the latitudes of the Antarctic circumpolar current (ACC)^{19,21}. The timescale on which newly formed North Atlantic deep water is exported to the Southern Ocean is similarly around several centuries²². The bipolar seesaw relationship observed between ice core records potentially bears the imprint of both atmospheric and oceanic teleconnections; precise constraints on the interhemispheric phasing can help distinguish which mode dominates, and can also identify leads and lags^{10,19,21}.

Completed in December 2011, the West Antarctic Ice Sheet (WAIS) Divide ice core (WDC)¹⁷ was drilled and recovered to a depth of 3,405 m. Here we present results from the deep part of the core (Fig. 1), extending back to 68 kyr before 1950 (before present; BP). The WDC climatic records show no stratigraphic disturbances (such as large-scale folds) that are commonly encountered near the base of ice cores, a fact we attribute to basal melting at the site that removes old ice before such disturbances can develop and that decreases shear stress by lubricating the bed. The Greenland NGRIP core similarly has strong basal melting and an undisturbed stratigraphy¹. WDC $\delta^{18}\text{O}$ of ice, a proxy for local condensation temperature, exhibits clear millennial-scale variability as observed across the Antarctic continent (Fig. 1c, d). We evaluate the phasing of WDC millennial variability relative to $\delta^{18}\text{O}$ of the Greenland NGRIP core (Fig. 1a). For each Greenland Dansgaard–Oeschger (DO) event we can identify a corresponding Antarctic Isotopic Maximum (AIM) event³, although AIM 9 is only very weakly expressed in WDC (we adopt the naming convention whereby AIM x is concomitant with DO x).

To investigate the phasing of the bipolar seesaw, we have synchronized WDC to the Greenland NGRIP core by means of globally well-mixed atmospheric methane (CH_4 ; Fig. 1b)^{2,23}. WDC allows CH_4 synchronization at unprecedented, sub-centennial precision as a result of the small difference between gas age and ice age (Δage) and continuous, centimetre-scale resolution CH_4 record (Extended Data Figs 1 and 2). Because uncertainties in the relative phasing of CH_4 and Greenland climate²⁴ are smaller than uncertainties in Greenland Δage , we synchronize WDC CH_4 directly to NGRIP $\delta^{18}\text{O}$ (rather than to NGRIP CH_4)²³.

As pointed out by several authors^{6,21}, a strong anti-correlation exists between Greenland $\delta^{18}\text{O}$ and the rate of change (that is, the first time derivative) of Antarctic $\delta^{18}\text{O}$. This relationship is consistent with a simple thermodynamic model of the bipolar seesaw in which Antarctic temperature variations are moderated by the large thermal mass of the

*Lists of participants and their affiliations appear at the end of the paper.

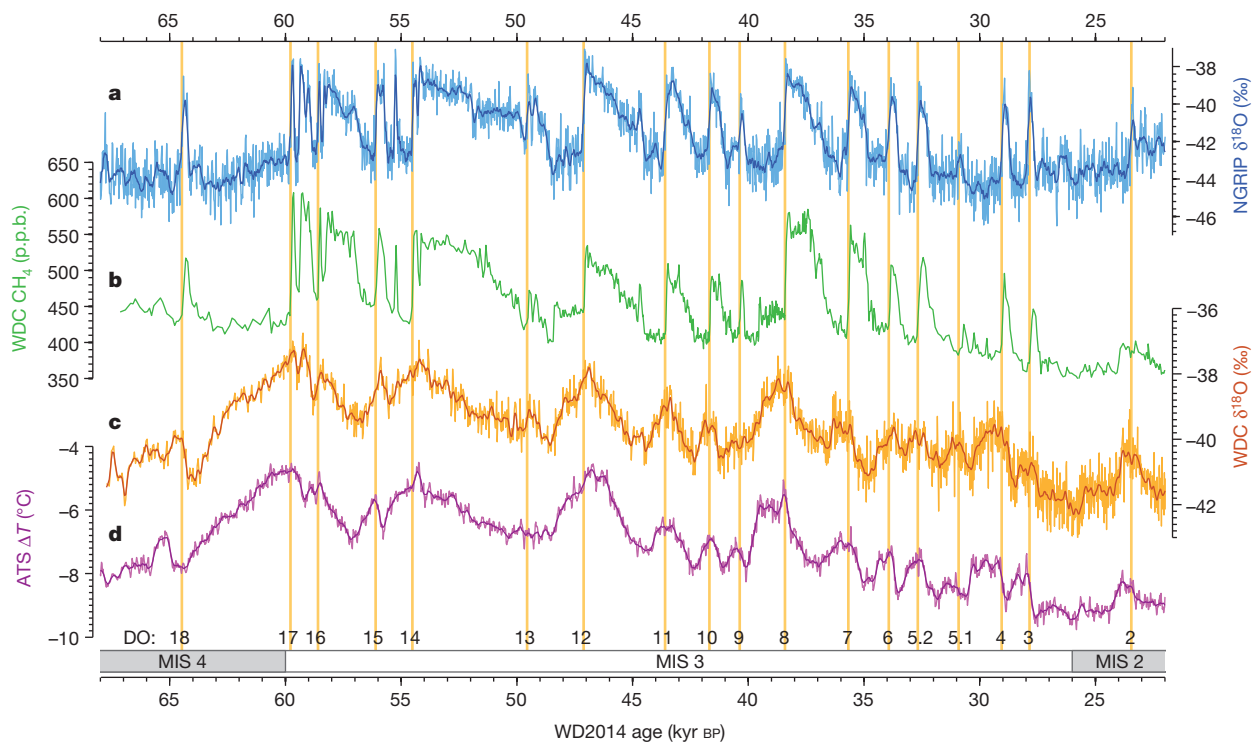


Figure 1 | Records of glacial abrupt millennial-scale climatic variability. **a**, Greenland NGRIP $\delta^{18}\text{O}$ record¹ on GICC05 \times 1.0063 chronology (Methods). **b**, WDC discrete CH_4 record on the WD2014 chronology, which is based on layer counting (0–31.2 kyr) and CH_4 synchronization to NGRIP

(31.2–68 kyr)²³. **c**, WDC $\delta^{18}\text{O}$ record. **d**, Antarctic temperature stack (ATS)³⁰ in degrees Celsius relative to the present day on AICC12 \times 1.0063 chronology. DO/AIM events are indicated with orange vertical bars, numbered at the bottom of the figure.

Southern Ocean⁶. In evaluating this relationship at WAIS Divide (Fig. 2a, blue curve), we find the strongest anti-correlation at a NH lead of about 170 years (blue dot in Fig. 2a). This timing is distinct from the zero-year lead commonly assumed in mathematical descriptions of the bipolar seesaw. The analysis is repeated using an ensemble of 4×10^3 alternative WDC chronologies (Methods), showing that the centennial-scale timing is a robust result (Fig. 2d) with an estimated uncertainty of 69 years (2σ uncertainty bounds are used throughout this work). Evaluation of the cross-correlations using WDC CH_4 instead of NGRIP $\delta^{18}\text{O}$ gives almost identical results (Fig. 2a, green curve), in line with the notion that CH_4 is a good proxy for Greenland climate².

Next we analyse the DO–AIM coupling in more detail. The bipolar seesaw theory suggests that during Greenland stadial periods heat accumulates in the SH, causing gradual warming of Antarctica; during interstadial periods Antarctica is cooling. The abrupt stadial–interstadial transitions in Greenland are accompanied by a breakpoint in the WDC $\delta^{18}\text{O}$ record, where the warming trend changes to a cooling trend. Although the timing of abrupt transitions can be established unambiguously in both CH_4 and Greenland $\delta^{18}\text{O}$ records, the smaller signal-to-noise ratio of Antarctic $\delta^{18}\text{O}$ time series complicates breakpoint identification for individual AIM events. To overcome this limitation, we stack and average the AIM events to detect their shared climatic signal (Methods and Extended Data Figs 3 and 4). We align WDC records at the midpoint of the DO CH_4 transitions, which is set to lag the midpoint in the NGRIP $\delta^{18}\text{O}$ transition by 56 ± 38 years²⁴. The relative timing of the WDC $\delta^{18}\text{O}$ and CH_4 curves is determined by Δ_{age} , which is the largest source of uncertainty (Methods).

We find that Antarctic cooling is delayed relative to abrupt NH warming by 218 ± 92 years on average (Fig. 2b, e); similarly, Antarctic warming lags NH cooling by 208 ± 96 years (Fig. 2c, f). The robustness of this result is demonstrated with a Monte Carlo analysis in which we randomly perturb the relative alignment of the individual AIM events, in combination with an ensemble of 4×10^3

alternative WDC chronologies. The timing of the WDC $\delta^{18}\text{O}$ breakpoint (orange dots in Fig. 2b, c) is determined by using an automated fitting algorithm (Methods and Extended Data Fig. 5). Performing the analysis separately on a stack of only the major AIM events (AIM 4, 8, 12, 14 and 17), only the minor AIM events or stacks of eight randomly selected AIM events gives nearly identical phasing (Extended Data Fig. 6), excluding the possibility that the result is dominated by the timing of a few prominent events. We repeat the stacking procedure for the WDC sea-salt sodium record (Extended Data Fig. 7), and find that this tracer, which has been interpreted as a proxy for sea-ice production²⁵, changes almost synchronously with WDC $\delta^{18}\text{O}$ —possibly reflecting a common forcing by Southern Ocean temperatures⁶.

At the onset of the NH Bølling warm period (DO 1; 14.6 kyr) we find a north–south phasing comparable to that of the glacial period, with a 256 ± 133 -year lag of the Antarctic $\delta^{18}\text{O}$ response (Fig. 3 and Extended Data Table 1). The inter-polar phasing at the onset and termination of the Younger Dryas stadial is ambiguous in our record (Extended Data Table 1), mostly because of the relatively gradual nature of the Younger Dryas onset and the presence of two local maxima in the WAIS-D $\delta^{18}\text{O}$ record around the Younger Dryas–Holocene transition (possibly reflecting regional climate). A recent study using a CH_4 -synchronized stack of five near-coastal Antarctic cores spanning the deglaciation suggested a near synchrony of Antarctic breakpoints and Greenland transitions within a dating uncertainty of 200 years¹⁰. Our result overlaps with this range. However, the much smaller dating uncertainty at WDC and our use of the full sequence of glacial AIM events shows that a centennial-scale Antarctic lag is a systematic feature of DO–AIM coupling throughout the glacial period.

The lead of NH climate revealed at WDC (Fig. 2) provides clues about DO climate dynamics. The simplest interpretation is that the abrupt phases of the DO cycle are initiated in the NH, presumably in the North Atlantic. This is consistent with several proposed DO mechanisms, such as North Atlantic sea-ice dynamics⁹, freshwater

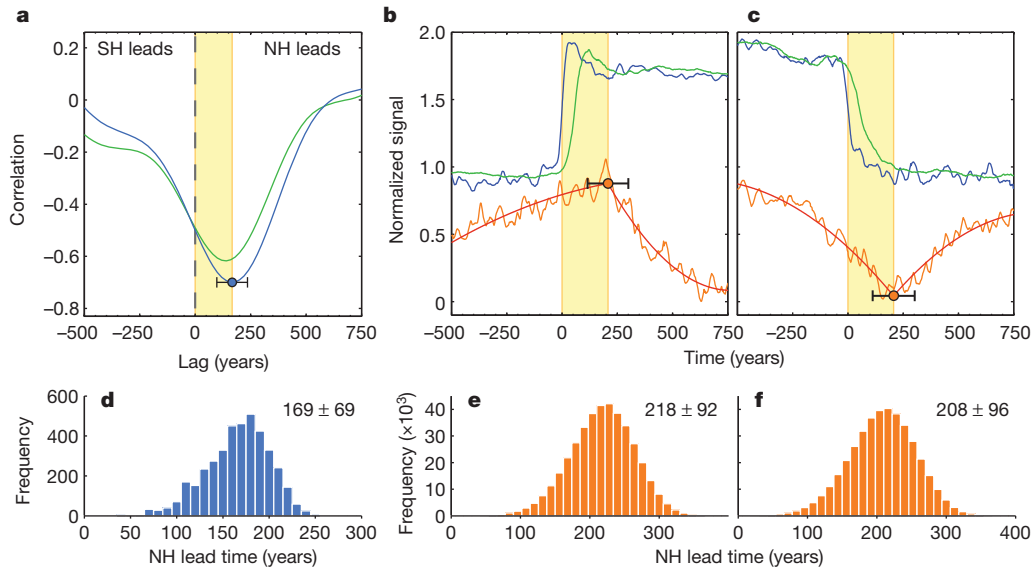


Figure 2 | Interhemispheric phasing of the bipolar seesaw. **a**, Lagged correlation between NGRIP $\delta^{18}\text{O}$ and WDC $d(\delta^{18}\text{O})/dt$ (blue), and between WDC CH_4 and $d(\delta^{18}\text{O})/dt$ (green). Millennial-scale variability is isolated by using a fourth-order Butterworth bandpass filter (500–10,000-year window); the CH_4 -synchronized part of the records is used (31.2–68 kyr). **b**, DO 3–18 stack of NGRIP $\delta^{18}\text{O}$ (blue), WDC CH_4 (green) and WDC $\delta^{18}\text{O}$ (orange with curve fit), aligned at the midpoint of the DO warming signal. Events are averaged with their original amplitudes and normalized after stacking for

convenience of visualization. **c**, As in **b**, but for NH abrupt cooling events (that is, the interstadial terminations). **d–f**, Histograms of NH lead time associated with **a–c**, respectively, generated by binning solutions from the sensitivity study. The total number of solutions is 4×10^3 in **d**, and 4×10^5 in **e** and **f**. Distribution mean and 2σ probability bounds are listed in the panels. Shaded vertical yellow bars (upper panels) show NH lead time; the error bar represents 2σ as defined for the lower panels.

forcing⁸ or ice shelf collapse⁷. We acknowledge, however, that the abrupt North Atlantic events could be the response to a remote process not visible in the ice core records; therefore, although we cannot ascertain the location of the elusive DO ‘trigger’ (if such a concept is even meaningful in a highly coupled dynamical system), our results clearly indicate a north-to-south directionality of the abrupt phases of the bipolar seesaw signal.

The centennial timescale of the NH lead demonstrates the dominance of oceanic processes in propagating NH temperature anomalies to the SH high latitudes. Any atmospheric teleconnection would be manifested within at most a few decades after the abrupt NH event¹⁸; on this timescale the WDC $\delta^{18}\text{O}$ stacks (Fig. 2b, c) show no discernible temperature response above the noise. We estimate the noise level by subtracting the fitted curves from the $\delta^{18}\text{O}$ stacks; the remaining signal has a 2σ variability of 0.14‰, or about 0.18 °C assuming an isotope sensitivity of 0.8‰ K^{-1} . We therefore estimate an upper bound of 0.18 °C on an atmospherically induced Antarctic temperature response (for comparison, millennial Antarctic temperature variations are on the order of 1–2 °C). A readjustment of atmospheric transport may induce spatially inhomogeneous temperature changes^{8,16} that may be (partly) responsible for the heterogeneity in expression, or shape, of AIM events across Antarctica³.

We find that on average the DO cooling signal is transmitted as fast to Antarctica as the DO warming signal is (our sensitivity study suggests a difference in propagation time of 10 ± 89 years). This implies that the north-to-south propagation time is independent of the AMOC background state; that is, it is independent of whether the AMOC is in the weak or strong overturning state. Modelling work suggests that the meridional propagation time across the ACC latitudes depends primarily on ACC strength²¹; our inference of similar propagation times may thus reflect a stability of the ACC on millennial timescales. There is also a conspicuous synchronicity between the phasing of the bipolar seesaw and the duration of the abrupt increase in CO_2 at 14.6 kyr (Fig. 3d); if the former does indeed reflect the timescale of the oceanic response, this may hold clues about the (unidentified) source of this CO_2 (ref. 26).

Proxy records of North Atlantic ventilation and overturning strength during Marine Isotope Stage 3 typically show the most prominent excursions during Heinrich stadials^{11,12}, periods of extreme cold in the North Atlantic associated with layers of ice-rafted debris in ocean sediments that represent times of massive delivery of

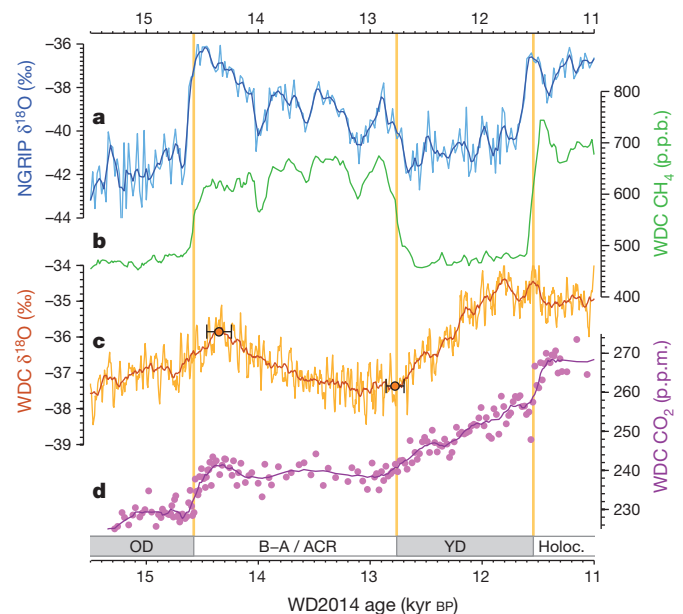


Figure 3 | Timing of the last deglaciation. **a**, NGRIP $\delta^{18}\text{O}$ on GICC05 chronology¹. **b**, WDC CH_4 . **c**, WDC $\delta^{18}\text{O}$ with breakpoints as orange dots and error bars showing the 2σ uncertainty bounds (Extended Data Table 1). **d**, WDC CO_2 data (dots) with spline fit (solid line)²⁶. Period abbreviations: OD, Oldest Dryas; B–A / ACR, Bølling–Allerød; YD, Younger Dryas; Holoc., Holocene. Vertical orange lines correspond to the midpoints of the WDC CH_4 transitions. NGRIP and WDC chronologies are both based on annual-layer counting, and are fully independent.

debris-laden icebergs (Heinrich events). This suggests that there may be a difference between climate dynamics during Heinrich and non-Heinrich stadials. We find no anomalous NH lead time for DO transitions directly after or before Heinrich stadials (Extended Data Fig. 6), and thus no evidence that Heinrich stadials are unusual from the perspective of the oceanic teleconnections that dominate the bipolar seesaw. Similarly, previous work has shown that an increase in Antarctic temperature is linearly related to Greenland stadial duration, irrespective of the occurrence of Heinrich events during these stadials⁵. Recent studies suggest that decreases in AMOC strength precede the Heinrich events, allowing the possibility that the latter are a response to AMOC variations rather than their cause^{27,28}. The main influence of Heinrich events on the bipolar seesaw may thus be to lengthen the stadial periods during which they occur by suppressing the AMOC by means of iceberg-delivered freshwater, allowing large amounts of heat to build up in the Southern Ocean.

Although both the data⁵ and the models^{19,21} suggest a fast temperature response in the South Atlantic (decadal-scale in models), there is currently no consensus in existing model studies on the physical mechanisms and timescales of the processes that propagate temperature signals between the South Atlantic and the Southern Ocean; complicating factors to consider include the lack of a zonal boundary to support the propagation of Kelvin waves²¹, the large thermal inertia of the Southern Ocean⁶, the complexity of eddy heat transport across the Antarctic circumpolar current, and the coupling between the extent of Antarctic sea ice and the overturning circulation²⁹. In this context, our precise phasing observations provide a new constraint with which to test future model simulations seeking to capture the dynamics of millennial-scale climate variability.

Online Content Methods, along with any additional Extended Data display items and Source Data, are available in the online version of the paper; references unique to these sections appear only in the online paper.

Received 11 September 2014; accepted 3 March 2015.

1. NGRIP Project Members. High-resolution record of Northern Hemisphere climate extending into the last interglacial period. *Nature* **431**, 147–151 (2004).
2. Blunier, T. & Brook, E. J. Timing of millennial-scale climate change in Antarctica and Greenland during the last glacial period. *Science* **291**, 109–112 (2001).
3. EPICA Community Members. One-to-one coupling of glacial climate variability in Greenland and Antarctica. *Nature* **444**, 195–198 (2006).
4. Crowley, T. J. North Atlantic Deep Water cools the southern hemisphere. *Paleoceanography* **7**, 489–497 (1992).
5. Barker, S. *et al.* Interhemispheric Atlantic seesaw response during the last deglaciation. *Nature* **457**, 1097–1102 (2009).
6. Stocker, T. F. & Johnsen, S. J. A minimum thermodynamic model for the bipolar seesaw. *Paleoceanography* **18**, 1087 (2003).
7. Petersen, S. V., Schrag, D. P. & Clark, P. U. A new mechanism for Dansgaard-Oeschger cycles. *Paleoceanography* **28**, 24–30 (2013).
8. Rind, D. *et al.* Effects of glacial meltwater in the GISS coupled atmosphere–ocean model. 2. A bipolar seesaw in Atlantic Deep Water production. *J. Geophys. Res.* **106** (D21) 27355–27365 (2001).
9. Dokken, T. M., Nisanoglu, K. H., Li, C., Battisti, D. S. & Kissel, C. Dansgaard-Oeschger cycles: interactions between ocean and sea ice intrinsic to the Nordic seas. *Paleoceanography* **28**, 491–502 (2013).
10. Pedro, J. B. *et al.* The last deglaciation: timing the bipolar seesaw. *Clim. Past* **7**, 671–683 (2011).
11. Piotrowski, A. M., Goldstein, S. L., Hemming, S. R., Fairbanks, R. G. & Zyllberg, D. R. Oscillating glacial northern and southern deep water formation from combined neodymium and carbon isotopes. *Earth Planet. Sci. Lett.* **272**, 394–405 (2008).
12. Martrat, B. *et al.* Four climate cycles of recurring deep and surface water destabilizations on the Iberian margin. *Science* **317**, 502–507 (2007).
13. Peterson, L. C., Haug, G. H., Hughen, K. A. & Röhl, U. Rapid changes in the hydrologic cycle of the tropical Atlantic during the last glacial. *Science* **290**, 1947–1951 (2000).
14. Chiang, J. C. H. & Bitz, C. M. Influence of high latitude ice cover on the marine Intertropical Convergence Zone. *Clim. Dyn.* **25**, 477–496 (2005).
15. Toggweiler, J. R. & Lea, D. W. Temperature differences between the hemispheres and ice age climate variability. *Paleoceanography* **25**, PA2212 (2010).
16. Timmermann, A. *et al.* Towards a quantitative understanding of millennial-scale Antarctic warming events. *Quat. Sci. Rev.* **29**, 74–85 (2010).
17. WAIS Divide Project Members. Onset of deglacial warming in West Antarctica driven by local orbital forcing. *Nature* **500**, 440–444 (2013).
18. Vellinga, M. & Wood, R. A. Global climatic impacts of a collapse of the Atlantic thermohaline circulation. *Clim. Change* **54**, 251–267 (2002).
19. Liu, Z. Y. & Alexander, M. Atmospheric bridge, oceanic tunnel, and global climatic teleconnections. *Rev. Geophys.* **45**, RG2005 (2007).
20. Masuda, S. *et al.* Simulated rapid warming of abyssal North Pacific waters. *Science* **329**, 319–322 (2010).
21. Schmittner, A., Saenko, O. A. & Weaver, A. J. Coupling of the hemispheres in observations and simulations of glacial climate change. *Quat. Sci. Rev.* **22**, 659–671 (2003).
22. England, M. H. The age of water and ventilation timescales in a global ocean model. *J. Phys. Oceanogr.* **25**, 2756–2777 (1995).
23. Buizert, C. *et al.* The WAIS Divide deep ice core WD2014 chronology. Part 1. Methane synchronization (68–31 ka BP) and the gas age–ice age difference. *Clim. Past* **11**, 153–173 (2015).
24. Baumgartner, M. *et al.* NGRIP CH₄ concentration from 120 to 10 kyr before present and its relation to a $\delta^{15}\text{N}$ temperature reconstruction from the same ice core. *Clim. Past* **10**, 903–920 (2014).
25. Wolff, E. W., Rankin, A. M. & Röthlisberger, R. An ice core indicator of Antarctic sea ice production? *Geophys. Res. Lett.* **30**, 2158 (2003).
26. Marcott, S. A. *et al.* Centennial-scale changes in the global carbon cycle during the last deglaciation. *Nature* **514**, 616–619 (2014).
27. Gutjahr, M. & Lippold, J. Early arrival of Southern Source Water in the deep North Atlantic prior to Heinrich event 2. *Paleoceanography* **26**, PA2101 (2011).
28. Marcott, S. A. *et al.* Ice-shelf collapse from subsurface warming as a trigger for Heinrich events. *Proc. Natl Acad. Sci. USA* **108**, 13415–13419 (2011).
29. Ferrari, R. *et al.* Antarctic sea ice control on ocean circulation in present and glacial climates. *Proc. Natl Acad. Sci. USA* **111**, 8753–8758 (2014).
30. Parrenin, F. *et al.* Synchronous change of atmospheric CO₂ and Antarctic temperature during the last deglacial warming. *Science* **339**, 1060–1063 (2013).

Supplementary Information is available in the online version of the paper.

Acknowledgements We thank the WAIS Divide Drilling Team (2006–2013) (E. Morton, P. Cassidy, M. Jayred, J. Robinson, S. Polishinski, J. Koehler, L. Albershardt, J. Goetz, B. Gross, R. Kulin, S. Haman, W. Neumeister, C. Zander, J. Kyne, L. Augustin, B. Folmer, S. B. Hansen, E. Alexander and J. Fowler) and the dozens of core handlers who processed the ice core in the field and at the National Ice Core Laboratory (NICL). This work is funded through the US National Science Foundation grants 0944078, 0841308 (to M.A.), 1043528 (to R.B.A., D.E.V. and J.M.F.), 1142173 (to R.B.), 1204172, 1142041, 1043518 (to E.J.B.), 0839066 (to J.C.-D.), 0087345, 0944191 (to H.C. and E.D.W.), 0539232, 0537661 (to K.M.C.), 1142069, 1142115 (to N.W.D.), 0841135 (to IDDO), 0839093, 1142166 (to J.R.M.), 0440819, 1142164 (to K.C.M.), 1142178 (to P.B.P.), 0538657 (to J.P.S.), 1043500, 0944584 (to T.A.S.), 1043313 (to M.K.S.), 0537930, 1043092 (to E.J.S.), 0230149, 0230396, 0440817, 0440819, 0944191, 0944348 (to K.C.T.), 0944266 (to M.S.T.), 0839137 (to K.C.W. and K.N.), 0537593 and 1043167 (to J.W.C.W.); the USGS Climate and Land Use Change Program (to G.D.C. and J.J.F.); the NOAA Climate and Global Change Fellowship Program, administered by the University Corporation for Atmospheric Research (to C.B.); the Villum Foundation (to M.W.); the Joint Institute for the Study of the Atmosphere and Ocean (to J.B.P.); JISAO contribution no. 2343; and the Korea Polar Research Institute, grant PE15010 (to J.A.). The National Science Foundation Office of Polar Programs also funded the WAIS Divide Science Coordination Office at the Desert Research Institute of Nevada and University of New Hampshire for the collection and distribution of the WAIS Divide ice core and related tasks; the Ice Drilling Program Office and Ice Drilling Design and Operations group for coring activities; the NICL for curation of the core; Raytheon Polar Services for logistics support in Antarctica; and the 109th New York Air National Guard for airlift in Antarctica.

Author Contributions Data analysis and δ age modelling were performed by C.B.; annual-layer counting (dating) of upper 2,850 m by M.S., T.J.F., M.W., K.C.T. and K.M.C.; CH₄ synchronization (dating) of lower 555 m by C.B., K.M.C., J.P.S. and T.J.F.; age scale validation by N.W.D., N.I., K.C.W., K.N. and T.E.W.; discrete water isotope analysis by E.J.S., A.J.Sc. and S.W.S.; continuous water isotope analysis by J.W.C.W., T.R.J., B.H.V. and V.G.; discrete CH₄ analysis by T.A.S., L.E.M., J.E.L., J.S.E., J.L.R. and E.J.B.; continuous CH₄ analysis by R.H.R., E.J.B. and J.R.M.; CO₂ analysis by S.A.M., M.L.K., T.K.B., J.A. and E.J.B.; $\delta^{15}\text{N}$ of N₂ analysis by D.B., C.B., A.J.O. and J.P.S.; continuous-flow chemical analysis by M.S., O.J.M., N.J.C., D.R.P. and J.R.M.; discrete chemical analysis by J.C.-D., D.G.F., B.G.K., K.K. and G.J.W.; ice core physical properties by R.B.A., J.M.F., D.E.V., M.K.S. and J.J.F.; borehole logging by R.C.B. and G.D.C.; biological studies by J.C.P. and P.B.P.; temperature reconstructions by K.M.C. and G.D.C.; tephrochronology by N.W.D. and N.I.; firm studies by M.A., T.A.S. and S.G.; ¹⁰Be analysis by K.C.W. and T.E.W.; field science oversight, D.E.V. and B.H.V.; site selection by H.C., E.D.W. and E.C.P.; science management and sample distribution by M.S.T. and J.M.S.; logistics support, planning and management by M.J.K.; drilling management by A.J.Sh., C.R.B., D.A.L., and A.W.W.; deep drill design by A.J.Sh., J.A.J., N.B.M. and C.J.G.; drilling field management by J.A.J., K.R.S. and N.B.M.; sample collection and drill operations by C.J.G., J.J.G., T.W.K. and P.J.S. The field sample handling leaders were A.J.O., B.G.K., P.D.N. and G.J.W.; sample curation, processing and distribution was performed by G.M.H., B.A., R.M.N., E.C. and B.B.B.; the overall WAIS Divide Project design and management, Chief Scientist and field leader was K.C.T. The manuscript was written by C.B., E.J.S. and J.B.P. with assistance from J.P.S., B.R.M., E.J.B. and K.C.T.; all authors discussed the results and contributed to improving the final manuscript. Any use of trade, product, or firm names is for descriptive purposes only and does not imply endorsement by the US Government.

Author Information Reprints and permissions information is available at www.nature.com/reprints. The authors declare no competing financial interests. Readers are welcome to comment on the online version of the paper. Correspondence and requests for materials should be addressed to C.B. (buizert@science.oregonstate.edu).

WAIS Divide Project Members

Christo Buizert¹, Betty Adrian², Jinho Ahn³, Mary Albert⁴, Richard B. Alley⁵, Daniel Baggenstos⁶, Thomas K. Bauska¹, Ryan C. Bay⁷, Brian B. Bencivengo², Charles R. Bentley⁸, Edward J. Brook¹, Nathan J. Chellman⁹, Gary D. Clow¹⁰, Jihong Cole-Dai¹¹, Howard Conway¹², Eric Cravens¹³, Kurt M. Cuffey¹⁴, Nelia W. Dunbar¹⁵, Jon S. Edwards¹, John M. Fegyveresi⁵, Dave G. Ferris¹¹, Joan J. Fitzpatrick¹⁶, T. J. Fudge¹², Chris J. Gibson⁸, Vasileios Gkinis^{17,18}, Joshua J. Goetz⁸, Stephanie Gregory⁴, Geoffrey M. Hargreaves², Nels Iverson¹⁵, Jay A. Johnson⁸, Tyler R. Jones¹⁷, Michael L. Kalk¹, Matthew J. Kippenhan¹⁹, Bess G. Koffman²⁰, Karl Kreutz²¹, Tanner W. Kuhl⁸, Donald A. Lebar⁸, James E. Lee¹, Shaun A. Marcott^{1,22}, Bradley R. Markle¹², Olivia J. Maselli⁹, Joseph R. McConnell⁹, Kenneth C. McGwire⁹, Logan E. Mitchell¹, Nicolai B. Mortensen⁸, Peter D. Neff²³, Kunihiro Nishizumi²⁴, Richard M. Nunn², Anais J. Orsi^{6,25}, Daniel R. Pasteris⁹, Joel B. Pedro^{18,26}, Erin C. Pettit²⁷, P. Buford Price⁷, John C. Priscu²⁸, Rachael H. Rhodes¹, Julia L. Rosen¹, Andrew J. Schauer¹², Spruce W. Schoenemann¹², Paul J. Sendelbach⁸, Jeffrey P. Severinghaus⁵, Alexander J. Shturmakov⁸, Michael Sigl⁹, Kristina R. Slawny⁸, Joseph M. Souney²⁹, Todd A. Sowers⁵, Matthew K. Spencer³⁰, Eric J. Steig¹², Kendrick C. Taylor⁹, Mark S. Twickler²⁹, Bruce H. Vaughn¹⁷, Donald E. Voigt⁵, Edwin D. Waddington¹², Kees C. Welten²⁴, Anthony W. Wendricks⁸, James W. C. White¹⁷, Mai Winstrup^{12,18}, Gifford J. Wong³¹ & Thomas E. Woodruff³²

¹College of Earth, Oceanic and Atmospheric Sciences, Oregon State University, Corvallis, Oregon 97331, USA. ²US Geological Survey National Ice Core Laboratory, Denver, Colorado 80225, USA. ³School of Earth and Environmental Science, Seoul National University, Seoul 151-742, Korea. ⁴Thayer School of Engineering, Dartmouth College, Hanover, New Hampshire 03755, USA. ⁵Department of Geosciences, Pennsylvania State University, University Park, Pennsylvania 16802, USA. ⁶Scripps Institution of Oceanography, University of California at San Diego, La Jolla, California 92093, USA. ⁷Department of Physics, University of California at Berkeley, Berkeley, California 94720,

USA. ⁸Ice Drilling Design and Operations, University of Wisconsin-Madison, Madison, Wisconsin 53706, USA. ⁹Desert Research Institute, Nevada System of Higher Education, Reno, Nevada 89512, USA. ¹⁰US Geological Survey, Boulder, Colorado 80309, USA. ¹¹Department of Chemistry and Biochemistry, South Dakota State University, Brookings, South Dakota 57007, USA. ¹²Department of Earth and Space Sciences, University of Washington, Seattle, Washington 98195-1310, USA. ¹³ADC Management Services, Lakewood, Colorado 80226, USA. ¹⁴Department of Geography, University of California at Berkeley, Berkeley, California 94709, USA. ¹⁵Earth and Environmental Science Department, New Mexico Tech, Socorro, New Mexico 87801, USA. ¹⁶US Geological Survey, Denver, Colorado 80225, USA. ¹⁷Institute of Arctic and Alpine Research, University of Colorado, Boulder, Colorado 80309-0450, USA. ¹⁸Centre for ice and climate, University of Copenhagen, DK-2100 Copenhagen Ø, Denmark. ¹⁹Antarctic Support Contract, Lockheed Martin US Antarctic Program, Centennial, Colorado 80112, USA. ²⁰Lamont-Doherty Earth Observatory, Columbia University, Palisades, New York 10964, USA. ²¹Climate Change Institute and School of Earth and Climate Sciences, University of Maine, Orono, Maine 04469, USA. ²²University of Wisconsin-Madison, Madison, Wisconsin, Wisconsin 53706 USA. ²³Antarctic Research Centre, Victoria University of Wellington, Wellington 6012, New Zealand. ²⁴Space Sciences Laboratory, University of California at Berkeley, Berkeley, California 94720, USA. ²⁵Laboratoire des Sciences du Climat et de l'Environnement, Institut Pierre Simon Laplace, 91191 Gif-Sur-Yvette, France. ²⁶Joint Institute for the Study of the Atmosphere and Ocean, University of Washington, Seattle, Washington 98195, USA. ²⁷Department of Geosciences, University of Alaska Fairbanks, Fairbanks, Alaska 99775, USA. ²⁸Department of Land Resources and Environmental Sciences, Montana State University, Bozeman, Montana 59717, USA. ²⁹Institute for the Study of Earth, Oceans and Space, University of New Hampshire, Durham, New Hampshire 03824, USA. ³⁰School of Physical Sciences, Lake Superior State University, Sault Sainte Marie, Michigan 49783, USA. ³¹Department of Earth Sciences, Dartmouth College, Hanover, New Hampshire 03755, USA. ³²PRIME Laboratory, Purdue University, West Lafayette, Indiana 47907, USA.

METHODS

Core recovery and processing. The location of the WAIS Divide ice core (79.48° S, 112.11° W) was selected to provide the highest possible time-resolution record of Antarctic climate during the past 50 kyr or more, and to ensure that the record from the last deglaciation would not be in ice from the lower-quality brittle-ice zone¹⁷. The site has a present-day ice accumulation rate of 22 cm yr⁻¹, divide flow and an ice thickness of 3,460 m (J. Paden, personal communication 2011). No stratigraphic irregularities were detected in the core using visual observation, multitrack electrical conductivity measurements or gas stratigraphy. Coring was stopped 50 m above the bed to prevent contamination of the unfrozen basal environment. Drilling of the main core (WDC06A) started during the 2006/2007 field season and finished during the 2011/2012 field season, at the final depth of 3,405 m. Drilling was done with the US Deep Ice Sheet Coring (DISC) drill, a new drill designed and operated by the Ice Drilling Design and Operations group (engineering team at University of Wisconsin, Madison). Core handling and distribution of ice samples were performed by the National Ice Core Laboratory (US Geological Survey) and the Science Coordination Office (University of New Hampshire and Desert Research Institute). The drill and core handling methods had many innovations that improved core quality, especially in the brittle ice. These included improved mechanical characteristics of the drill, better control of the drilling operation, core handling procedures that minimized thermal and mechanical shock to core, netting to contain the brittle ice, and temperature tracking of all ice samples from the drill to the laboratories.

Data description. Water ¹⁸O/¹⁶O composition ($\delta^{18}\text{O}$) was measured at IsoLab, University of Washington, Seattle, Washington. Measurement procedures for WDC have been described elsewhere^{17,31}. In short, measurements were made at 0.5 m depth averaged resolution, using laser spectroscopy (Picarro L2120-*i* water isotope analyser). $\delta^{18}\text{O}$ data are reported relative to the VSMOW (Vienna Standard Mean Ocean water) standard, and normalized to the VSMOW-SLAP (Standard Light Antarctic Precipitation) scale.

Two separate data sets of atmospheric methane exist for WDC. The first is based on discrete sampling of the core; it was measured jointly at Penn State University (0–68 kyr, 0.5–2 m resolution) and at Oregon State University (11.4–24.8 kyr, 1–2 m resolution). For this record the air was extracted using a melt–refreeze technique from ~50 g ice samples, and analysed on a gas chromatograph with a flame ionization detector³². Corrections for gas solubility, blank and gravitational enrichment for the Oregon State University data were performed in accordance with ref. 33; corrections to the Penn State University data are described in ref. 17. A second data set (R. H. Rhodes, E. J. Brook, J. C. H. Chiang, T. Blunier, O. J. Maselli, J. R. McConnell, D. Romanini and J. P. Severinghaus, unpublished observations) is based on continuous flow analysis (CFA) in combination with laser spectroscopy^{34,35}. This data set, which is of higher temporal resolution, was used to determine the timing of the abrupt DO transitions (Extended Data Fig. 2). All CH₄ data are reported on the NOAA04 scale³⁶.

WDC Na concentrations were measured at the Ultra Trace Chemistry Laboratory at the Desert Research Institute, Reno, Nevada, by means of CFA. Sticks of ice were melted continuously on a heated plate. Potentially contaminated meltwater from the outer part of the ice stick was discarded. Two inductively coupled plasma mass spectrometers were used to analyse the stream of meltwater³⁷. The CFA chemistry and CH₄ data were measured simultaneously on the same ice samples, and all measurements are co-registered in depth.

Age scale and Δ age. For WDC we use the WD2014 chronology, which is based on annual-layer counting down to 2,850 m (31.2 kyr BP), and on stratigraphic matching by means of globally well-mixed methane for the deepest part of the core (2,850–3,405 m)²³. The deep section of the WD2014 chronology has been synchronized to a linearly scaled version of the layer-counted Greenland ice core chronology (GICC05). Multiplying the GICC05 chronology by 1.0063 brings the ages of abrupt DO events as observed in Greenland ice core records in agreement with the ages of these events observed in the U/Th-dated Hulu Cave speleothem record (which provides better absolute age control)²³. The NGRIP data in Fig. 1a have similarly been placed on the 1.0063 × GICC05 age scale; NGRIP data in Fig. 3a are plotted on the original GICC05 chronology.

WDC permits precise interhemispheric synchronization for two reasons. First, as a result of the high accumulation rates, Δ age remains relatively small. WDC Δ age is about an order of magnitude smaller than Δ age in cores from the East Antarctic Plateau, and about one-third of Δ age at other coastal sites that cover the last glacial period (Extended Data Fig. 1a)²³. As the uncertainty in Δ age is proportional to Δ age itself, this leads to smaller dating uncertainties at WDC. Second, recent technological developments in coupling laser spectrometers with ice core continuous-flow analysis³⁴ have resulted in a WDC CH₄ record with the highest temporal resolution of all Antarctic ice cores so far. Extended Data Fig. 2c compares the WDC CH₄ record (grey, ~2-year sampling resolution) with the EDML

CH₄ record (orange, ~100-year sampling resolution). The estimated uncertainty in WDC Δ age (ref. 23) is shown in Extended Data Fig. 1b–e.

Note that the transition between the layer-counted and CH₄-synchronized sections of the WD2014 chronology at 31.2 kyr does not influence our analysis of the bipolar seesaw phasing. In the stacking procedure we align each of the individual Antarctic events at the midpoint of the associated DO CH₄ transition. In doing so, we effectively synchronize all the WDC events to NGRIP $\delta^{18}\text{O}$, not just the events between 68 and 31.2 kyr. In performing the cross-correlation between NGRIP and WDC (Fig. 2a), we only analyse the CH₄-synchronized part of the record.

A dynamical version of the firn densification model^{23,38} is used to calculate the Δ age of the WD2014 chronology²³. We furthermore calculated WDC Δ age using an alternative firn densification model^{23,39,40} (Extended Data Fig. 1b, blue curve). Using this alternative Δ age scenario gives a NH lead time of 242 and 247 years for abrupt DO warming and DO cooling, respectively, in good agreement (within the 1 σ uncertainty bound) with results presented in the text.

Identification of abrupt DO transitions. We use the midpoint of the abrupt transitions as time markers to align individual events. The method for finding the midpoint is identical to that used in ref. 23, where further details can be found. The method is shown in Extended Data Fig. 2a, b for DO 17 and 16 (we use a recently proposed DO nomenclature⁴¹). For each transition we define a pre-transition level and a post-transition level (horizontal orange markers), and use linear interpolation to find the depth at which the tracer of interest ($\delta^{18}\text{O}$ or CH₄) has completed 25%, 50% and 75% of the pre-transition to post-transitional value. The 50% depth (red dots) is used to define the timing of the abrupt event; the 25% and 75% depths (blue dots) provide an uncertainty range on the midpoint²³.

It has been suggested that interhemispheric CH₄ synchronization is complicated by the fact that gas bubbles in ice cores have a gas age distribution, rather than a single age⁴². To investigate this effect at WDC, we construct a hypothetical gas age distribution (Extended Data Fig. 2d), using a (truncated) log-normal distribution as suggested elsewhere^{42,43}, in which we conservatively set $\sigma = 1$ and $\mu = \ln(50)$. The spectral width (or second moment) of this age distribution⁴⁴ is 24.3 years; for comparison, the gas-age spectral width for present-day WDC firn is only 4.8 years⁴⁵. Applying this filter to an atmospheric ramp in CH₄ (Extended Data Fig. 2e) shifts the midpoint of the transition (as recorded in the ice core) forwards by 5 years. Because we have conservatively chosen the age distribution to be very wide, this 5-year shift should be considered an upper bound. The influence of the gas age distribution on the transition midpoint identification is very small in comparison with other sources of uncertainty, and is neglected in the remainder of the manuscript.

Stacking procedure. We define a time vector τ that runs from time $t = -1,200$ to $t = 1,200$ in 1-year increments. Next, for each of the DO/AIM events, we set the midpoint of the NGRIP $\delta^{18}\text{O}$ transition to $t = 0$, and use linear interpolation to sample the different records onto time vector τ . For each individual DO/AIM event this results in a record that spans from $-1,200$ to $+1,200$ years relative to the abrupt transition, at annual time steps; we shall refer to these as the contributory records. To align the WDC records we set the midpoint in the WDC CH₄ transition to $t = 56$ years, using the observation that the CH₄ transition slightly lags the Greenland $\delta^{18}\text{O}$ signal^{23,24,46,47} (the uncertainty in this time lag is evaluated in the sensitivity study). With all the individual events synchronized and resampled to identical time spacing, we can average them to obtain the stacked record.

The spacing between DO events varies widely over time, ranging from several thousands of years to only hundreds of years. This means that in several cases the 2,400-year window we use contains more than a single event. We crop the contributory records whenever an adjacent event occurs within the sampling window (Extended Data Fig. 3). For widely spaced (that is, long-duration) events such as DO/AIM 12, no adjacent events fall within the time window, and no cropping is required (Extended Data Fig. 3a). For closely spaced events, such as DO/AIM 17.1, we need to crop neighbouring events (Extended Data Fig. 3b). The cropped parts of the contributory records are replaced with constant values that equal the boundary values (50-year averages) of the uncropped part of the record. The number of contributory records available as a function of time is shown in the bottom half of Extended Data Fig. 4. The shortest contributory record is the AIM 17.1 record, which is 700 years long.

Determining the breakpoint in the WDC $\delta^{18}\text{O}$ stack. We use an automated routine that is similar to the BREAKFIT algorithm⁴⁸, the main difference being the use of a second-order polynomial (rather than a linear) fit to the data, to account for the fact that the WDC $\delta^{18}\text{O}$ stack is curved rather than linear. The algorithm finds the breakpoint that minimizes the root mean square deviation (r.m.s.d.) between the stack (that is, the data) and the polynomial fit in the -600 to $+700$ years time interval (Extended Data Fig. 4); the interval was chosen

asymmetrically around zero to account for the fact that the breakpoint is always found at positive values. The routine operates as follows.

First, the user selects the range in which the algorithm is to look for the breakpoint, as well as a time step. For example, if the user selects 0–400 years at a 100-year time step, the algorithm will test the possibilities $t = 0, 100, 200, 300$ and 400 years. We shall refer to this one-dimensional array of values as the input vector.

Second, at each of the values in the input vector, the $\delta^{18}\text{O}$ stack is split into two pieces, and a second-order polynomial curve is fitted to data on each side separately. The two fitting curves are merged at their point of intersection. Note that the point of intersection can differ from the point where the data series were split into two.

Third, for each fit thus obtained, we calculate the r.m.s.d. to the stacked data over the -600 to $+700$ years time interval, and we select the best fit. The point of intersection of the two curves, rather than the point where the data series were split into two (that is, the values in the input vector), is considered the breakpoint in the $\delta^{18}\text{O}$ stack.

For most of the results in this work we let the algorithm search in the 0–400-year range, at a 2-year time step. The exception is the stacks of randomly selected DO events (Extended Data Fig. 6), for which we used a wider range (-100 to $+500$ years) to account for the larger spread in solutions. Note that the effective range of breakpoint detection is wider than the input range, because the point of intersection of the fitting curves is permitted to lie outside the range specified by the input vector. The fitting curves generated by the algorithm are plotted in dark orange lines in Fig. 2b, c and Extended Data Figs 4a, b, 6a–d and 7b, c; the breakpoint is indicated with an orange dot. The MATLAB code implementing the fitting procedure is provided in Supplementary Information.

The reason for using a quadratic rather than a linear fitting procedure is that Antarctic temperatures do not change in a linear fashion either before or after the abrupt transitions. As a test, we apply our fitting procedure to the WDC $\delta^{18}\text{O}$ stack (Fig. 2b), using either linear or quadratic fitting functions, in which we change the size of the data window from 300 years to 1,600 years. The window is applied symmetrically, meaning that equal numbers of years are used before and after the detected breakpoint (800 years on each side for a 1,600-year window). Data falling outside this window are ignored in the fitting procedure.

We find that the performance of the quadratic fitting procedure is superior in two important aspects (Extended Data Fig. 5). First, by using a quadratic fit, the breakpoint we detect is independent of the window size, which is not true for the linear fit. Second, the quadratic method provides a better approximation to the data, as expressed by the r.m.s.d. between the data and the fitting curve. At small window sizes of <700 years, both methods agree very well, and the fit to the data is comparable in terms of the r.m.s.d. This is due to the fact that at small window sizes the curvature of the time series is not very pronounced and is well approximated by a linear trend. We have also tested the BREAKFIT routine⁴⁸, which uses a linear fit on both sides of the breakpoint. We find a very good agreement between the breakpoints identified using the BREAKFIT routine and our linear fitting routine, with a mean difference of 0.2 years between them. Using a moving block bootstrap analysis⁴⁸, the BREAKFIT algorithm suggests a 2σ uncertainty of 50.8 years in breakpoint identification.

Monte Carlo sensitivity study. To assess how the different uncertainties in our method affect our conclusions, we perform a Monte Carlo sensitivity study. The largest source of uncertainty is the difference between gas age and ice age, or Δage (ref. 49). Δage determines the relative timing of the WDC CH_4 and $\delta^{18}\text{O}$ records, and thereby the phasing we infer for WDC AIM events relative to Greenland climate^{2,3,50}. Increasing Δage shifts WDC ice ages towards older ages, thereby decreasing the NH lead time that we infer; vice versa, decreasing Δage will shift the ice ages younger, increasing the observed NH lead time. The Δage reconstruction we use here is obtained from a dynamical firm-densification model^{40,47,51–54} constrained by $\delta^{15}\text{N}-\text{N}_2$ data, a proxy for past firm-column thickness⁵⁵. The firm-densification model results are in good agreement²³ with the alternative Δdepth method developed recently⁵⁶. For our current purpose we use an ensemble of 1,000 Δage histories (Extended Data Fig. 1b–e) generated by varying a suite of input parameters of the firm-densification model²³. We furthermore use four different depth–age interpolation strategies^{23,57}, providing a total of $1,000 \times 4 = 4,000$ alternative WDC chronologies.

For each of these 4,000 potential WDC chronologies we further perform a Monte Carlo simulation (100 realizations) in which we perturb the alignment of the contributory records. The rationale behind the Monte Carlo study is that there is an uncertainty in the synchronization of the contributory records, and we want to assess how this uncertainty impacts our conclusions. In the Monte Carlo study, a random timing error is assigned to each of the contributory records, and thereby they are effectively shifted relative to one another in time. We distinguish between systematic and non-systematic errors, in which the former are correlated between

the different AIM events, and the latter are not. Sensitivity tests with the firm densification model show that Δage is a systematic error; if we have overestimated glacial Δage by, for example, 50 years, this will probably be true for all of the AIM events. We consider five independent sources of uncertainty in the synchronization procedure.

First, the midpoint detection in the abrupt NGRIP $\delta^{18}\text{O}$ transitions has an uncertainty; we shift the record by a value drawn from a Gaussian distribution of zero mean and a width that equals the midpoint uncertainty as defined above. This error is non-systematic.

Second, as in the first point above, but for the midpoint in the abrupt WDC CH_4 transition.

Third, although all four interpolation strategies synchronize the abrupt NH warming events between NGRIP and WDC, only two of them synchronize the NH cooling events²³. For stacks of NH cooling we added an additional uncertainty drawn from a Gaussian distribution of zero mean and a width corresponding to the age difference between the cooling event as detected in NGRIP $\delta^{18}\text{O}$ and WDC CH_4 . This error is non-systematic.

Fourth, a recent extensive analysis suggests a lag of CH_4 behind Greenland $\delta^{18}\text{O}$ of 56 ± 38 years (2σ)²⁴. There are two types of uncertainty to consider: first, the CH_4 lag can differ between individual DO events (non-systematic error), and second, the central estimate of 56 years has an inherent uncertainty (systematic error). We here assume that both are equally large, and in the stacking procedure we assign both a 27-year systematic error and a 27-year non-systematic error to the CH_4 lag time. Both are drawn independently from a Gaussian distribution, and their combined uncertainty is therefore $(27^2 + 27^2)^{1/2} = 38$ years (that is, the 2σ uncertainty bound²⁴).

Fifth, the breakpoint fitting procedure has an intrinsic uncertainty. We estimate this by using the moving-block bootstrap analysis of the BREAKFIT algorithm⁴⁸, which suggests a 1σ uncertainty of 25.4 years (Extended Data Fig. 5a). We therefore apply a 50.8-year (2σ) systematic uncertainty (systematic because it applies to the full $\delta^{18}\text{O}$ stack rather than to individual events).

Each contributory record is then individually shifted by an amount that corresponds to the sum of the randomly assigned non-systematic errors. After realigning the contributory records in this manner, the entire stack is shifted in time by an amount that corresponds to the sum of randomly assigned systematic errors. We detect the breakpoint by using the fitting algorithm. For each of the 4,000 chronologies we test 100 realizations of the Monte Carlo realignment, thus obtaining a total of 4×10^5 ($1,000 \times 4 \times 100$) estimates of the WDC $\delta^{18}\text{O}$ breakpoint. No statistical methods were used to predetermine the sample size used in the Monte Carlo analysis. The outcome of the sensitivity study is presented in the histograms of Fig. 2e, f and Extended Data Fig. 6e–h.

The non-systematic errors, because they are independent of each other, accumulate slowly when added in quadrature. The systematic errors (such as the Δage uncertainty or the breakpoint fitting procedure) therefore dominate the final uncertainty estimate. Running the Monte Carlo experiment with Δage uncertainties withheld gives a 2σ uncertainty bound on the inter-polar phasing of 60 and 68 years for the DO onset and DO termination stacks, respectively; using only Δage uncertainties gives a 2σ uncertainty bound of 69 years. The Δage uncertainty is therefore as important as all other sources of uncertainty combined.

Code availability. The MATLAB code used to stack the records and perform the Monte Carlo analysis are provided in Supplementary Information.

Alternative stacks. To exclude the possibility that timing of the WDC $\delta^{18}\text{O}$ stack is dominated by a few prominent AIM events we perform the following tests.

First, we distinguish between major AIM events that are very prominent in the record, and minor events. The major AIM events are AIM 17, 14, 12, 8 and 4; all of these are preceded by NH Heinrich events. These large events have historically been called A-events, and are clearly visible even in low-resolution Antarctic cores (AIM 8, 12, 14 and 17 have been referred to in earlier work as A1, 2, 3 and 4, respectively)^{2,3}. The minor events are the remaining ones (AIM 3, 5.1, 5.2, 6, 7, 9, 10, 11, 13, 15, 16 and 18). When we compare a stack consisting of only the major AIM events with a stack of only the minor AIM events, we find no statistically significant difference in their timing (Extended Data Fig. 6a, b). The NH lead time for the major and minor AIM stacks is 230 ± 93 and 211 ± 94 years, respectively (Extended Data Fig. 6e, f); the timing of the full stack (218 ± 92 years) is intermediate to these values, as expected (Fig. 2b).

In a second experiment we randomly selected eight DO/AIM events in the stacking procedure for each of the 4×10^5 realizations of the Monte Carlo experiment; one such realization is shown in Extended Data Fig. 6c, d for abrupt NH warming and cooling, respectively. The NH lead time we find in this experiment is 210 ± 113 years and 208 ± 108 years for abrupt NH warming and cooling, respectively (Extended Data Fig. 6g, h). These mean values differ by only a few years from those found for the full WDC $\delta^{18}\text{O}$ stack (Fig. 2). Note that the distribution width of NH lead times in this experiment is wider than the

distribution width found for the full $\delta^{18}\text{O}$ stacks. The reason for this may be threefold: first, a stack with fewer contributory records has a smaller signal-to-noise ratio, making the breakpoint detection less certain; second, if the NH lead time differs slightly between the AIM events, the average timing of a randomly selected subset may differ from the average timing of the full set; and third, in the Monte Carlo procedure the contribution of non-systematic uncertainties scales roughly in proportion to \sqrt{N} , again suggesting a narrower distribution for higher N (the number of events in the stack). The wider distribution found on decreasing the number of events in the stack therefore does not represent a more realistic uncertainty bound on the phasing of the bipolar seesaw.

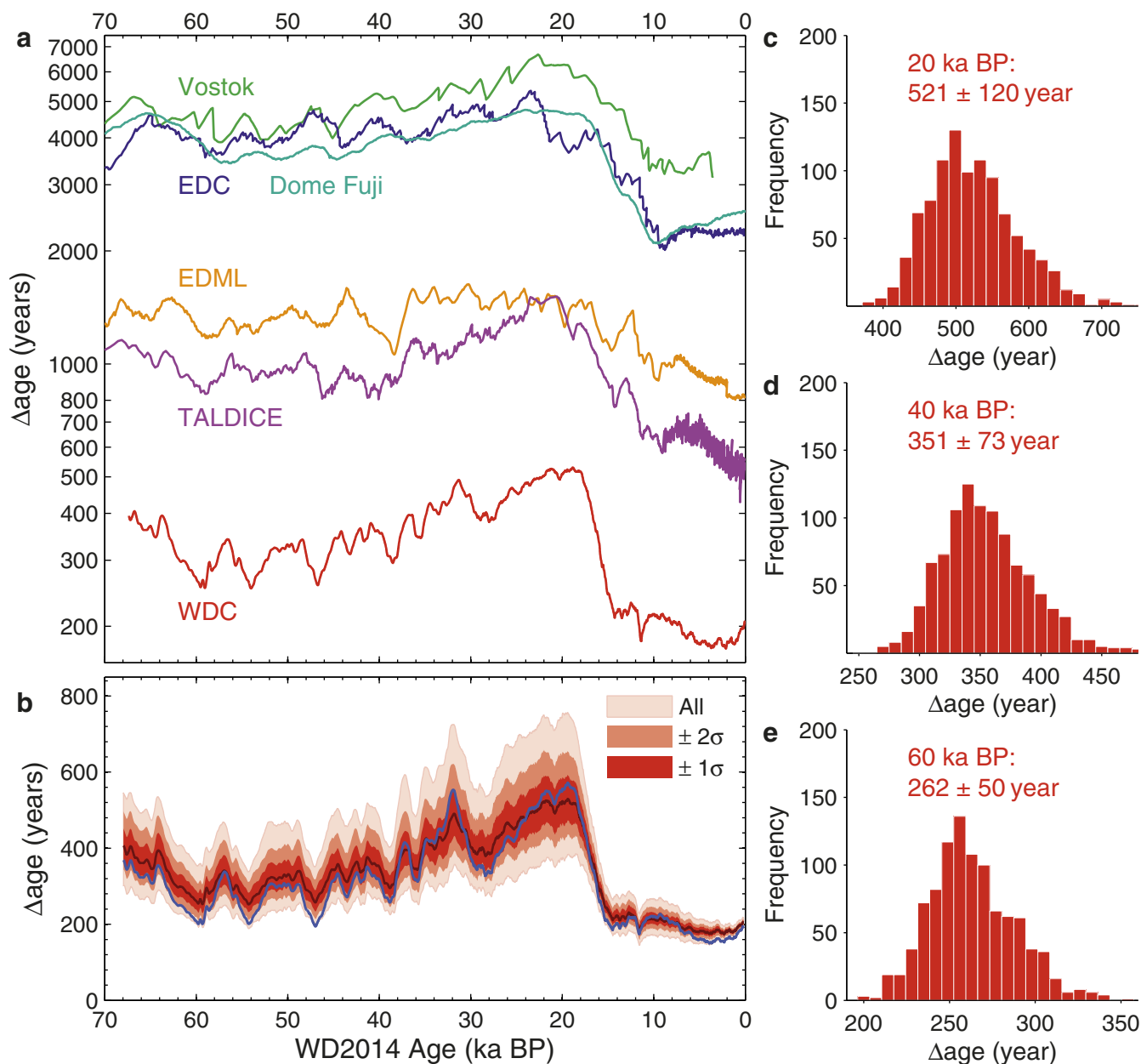
Stacking the WDC Na record. Last, we investigate the phasing of the WDC sea-salt Na (ssNa) record relative to Greenland and Antarctic climate. The sea-ice surface is a major source of sea-salt aerosols to the atmosphere around Antarctica, and consequently ssNa has been interpreted as a proxy for the production and extent of regional sea ice^{25,58,59}. Sea-salt Na is strongly anti-correlated with Antarctic climate on both orbital and millennial timescales^{58,60}.

Measured ssNa concentrations can be converted to a ssNa flux by multiplying with the accumulation rates at the site. On the East Antarctic plateau, the Na flux is expected to provide a better metric for atmospheric concentrations, because dry deposition dominates as a result of the very low accumulation rates⁵⁸. Accumulation rates are much higher at WAIS Divide, however, and Greenland ice cores provide a better analogue than those on the East Antarctic plateau. It has been shown at Greenland Summit⁶¹ that sea-salt concentrations in the ice reflect the atmospheric variations within 5%, whereas the sea-salt flux underestimates the atmospheric variations by about 50%. Thus, the observed variations in WDC ssNa concentrations should to first order reflect variations in the atmospheric loading.

We investigate the relative timing of the ssNa record with the same tools as those that we applied to the WDC $\delta^{18}\text{O}$ record. An evaluation of the lagged correlation between NGRIP $\delta^{18}\text{O}$ and the time derivative of the various WDC records is shown in Extended Data Fig. 7a. For ssNa we obtain a centennial-scale NH lead time, comparable to that observed for WDC $\delta^{18}\text{O}$. Stacking of the WDC impurity records yields the same picture (Extended Data Fig. 7b, c); the breakpoint in the ssNa stacks coincides with the breakpoint in the WDC $\delta^{18}\text{O}$ stack, and lags the abrupt NH transition by roughly two centuries. Note that because $\delta^{18}\text{O}$ and ssNa are both measured in the ice phase, the uncertainty that we estimate for the timing of the $\delta^{18}\text{O}$ breakpoint (2σ of about 90 years) also holds for the impurity records.

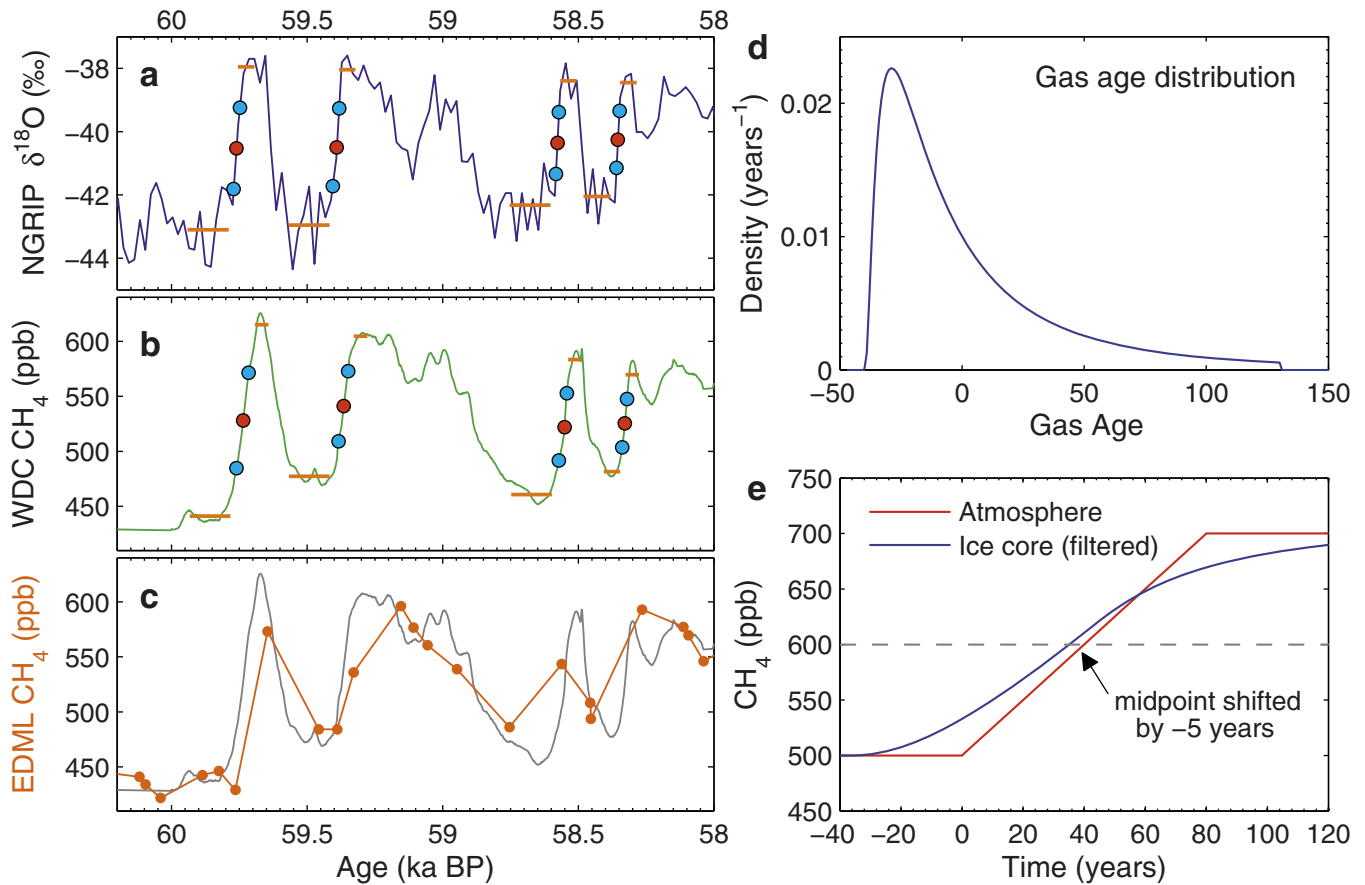
The synchronicity of WDC ssNa and $\delta^{18}\text{O}$ variations suggests that Antarctic climate and sea-ice extent are closely linked on centennial, or perhaps even sub-centennial timescales. This may reflect a common forcing and/or a feedback between Southern Ocean surface temperatures and sea-ice extent. The sea-ice extent may furthermore be important in forcing Antarctic temperatures (and $\delta^{18}\text{O}$)^{6,62}, particularly at the WAIS Divide site, where the marine influence is stronger than on the East Antarctic plateau¹⁷.

31. Steig, E. J. *et al.* Recent climate and ice-sheet changes in West Antarctica compared with the past 2,000 years. *Nature Geosci.* **6**, 372–375 (2013).
32. Sowers, T. *et al.* An interlaboratory comparison of techniques for extracting and analyzing trapped gases in ice cores. *J. Geophys. Res.* **102**, 26527–26538 (1997).
33. Mitchell, L. E., Brook, E. J., Sowers, T., McConnell, J. R. & Taylor, K. Multidecadal variability of atmospheric methane, 1000–1800 C.E. *J. Geophys. Res.* **116**, G02007 (2011).
34. Stowasser, C. *et al.* Continuous measurements of methane mixing ratios from ice cores. *Atmos. Meas. Tech.* **5**, 999–1013 (2012).
35. Rhodes, R. H. *et al.* Continuous methane measurements from a late Holocene Greenland ice core: atmospheric and in-situ signals. *Earth Planet. Sci. Lett.* **368**, 9–19 (2013).
36. Dlugokencky, E. *et al.* Conversion of NOAA atmospheric dry air CH_4 mole fractions to a gravimetrically prepared standard scale. *J. Geophys. Res.* **110**, D18306 (2005).
37. Sigl, M. *et al.* A new bipolar ice core record of volcanism from WAIS Divide and NEEM and implications for climate forcing of the last 2000 years. *J. Geophys. Res. Atmos.* **118**, 1151–1169 (2013).
38. Herron, M. M. & Langway, C. C. Firn densification: an empirical model. *J. Glaciol.* **25**, 373–385 (1980).
39. Arnaud, L., Barnola, J. M. & Duval, P. in *Physics of Ice Core Records* (ed. Hondoh, T.) 285–305 (Hokkaido Univ. Press, 2000).
40. Goujon, C., Barnola, J. M. & Ritz, C. Modeling the densification of polar firn including heat diffusion: application to close-off characteristics and gas isotopic fractionation for Antarctica and Greenland sites. *J. Geophys. Res.* **108** (D24), 4792 (2003).
41. Rasmussen, S. O. *et al.* A stratigraphic framework for abrupt climatic changes during the Last Glacial period based on three synchronized Greenland ice-core records: refining and extending the INTIMATE event stratigraphy. *Quat. Sci. Rev.* **106**, 14–28 (2014).
42. Köhler, P. Rapid changes in ice core gas records. Part 1. On the accuracy of methane synchronisation of ice cores. *Clim. Past Discuss.* **6**, 1453–1471 (2010).
43. Köhler, P., Fischer, H. & Schmitt, J. Atmospheric $\delta^{13}\text{C}$ and its relation to pCO_2 and deep ocean $\delta^{13}\text{C}$ during the late Pleistocene. *Paleoceanography* **25**, PA1213 (2010).
44. Trudinger, C. M. *et al.* Reconstructing atmospheric histories from measurements of air composition in firn. *J. Geophys. Res.* **107** (D24) 4780 (2002).
45. Battle, M. O. *et al.* Controls on the movement and composition of firn air at the West Antarctic Ice Sheet Divide. *Atmos. Chem. Phys.* **11**, 11007–11021 (2011).
46. Huber, C. *et al.* Isotope calibrated Greenland temperature record over Marine Isotope Stage 3 and its relation to CH_4 . *Earth Planet. Sci. Lett.* **243**, 504–519 (2006).
47. Rasmussen, S. O. *et al.* A first chronology for the North Greenland Eemian Ice Drilling (NEEM) ice core. *Clim. Past* **9**, 2713–2730 (2013).
48. Mudelsee, M. Break function regression. *Eur. Phys. J. Spec. Top.* **174**, 49–63 (2009).
49. Schwander, J. & Stauffer, B. Age difference between polar ice and the air trapped in its bubbles. *Nature* **311**, 45–47 (1984).
50. Capron, E. *et al.* Synchronising EDML and NorthGRIP ice cores using $\delta^{18}\text{O}$ of atmospheric oxygen ($\delta^{18}\text{O}_{\text{atm}}$) and CH_4 measurements over MIS5 (80–123 kyr). *Quat. Sci. Rev.* **29**, 222–234 (2010).
51. Barnola, J. M., Pimienta, P., Raynaud, D. & Korotkevich, Y. S. CO_2 -climate relationship as deduced from the Vostok ice core: a re-examination based on new measurements and on a re-evaluation of the air dating. *Tellus* **43**, 83–90 (1991).
52. Schwander, J. *et al.* Age scale of the air in the summit ice: implication for glacial-interglacial temperature change. *J. Geophys. Res.* **102**, 19483–19493 (1997).
53. Seierstad, I. *et al.* Consistently dated records from the Greenland GRIP, GISP2 and NGRIP ice cores for the past 104 ka reveal regional millennial-scale isotope gradients with possible Heinrich Event imprint. *Quat. Sci. Rev.* **106**, 29–46 (2014).
54. Buizert, C. *et al.* Greenland temperature response to climate forcing during the last deglaciation. *Science* **345**, 1177–1180 (2014).
55. Sowers, T., Bender, M., Raynaud, D. & Korotkevich, Y. S. $\delta^{15}\text{N}$ of N_2 in air trapped in polar ice: a tracer of gas transport in the firn and a possible constraint on ice age-gas age differences. *J. Geophys. Res.* **97**, 15683–15697 (1992).
56. Parrenin, F. *et al.* On the gas-ice depth difference (Δdepth) along the EPICA Dome C ice core. *Clim. Past* **8**, 1239–1255 (2012).
57. Fudge, T. J., Waddington, E. D., Conway, H., Lundin, J. M. D. & Taylor, K. Interpolation methods for Antarctic ice-core timescales: application to Byrd, Siple Dome and Law Dome ice cores. *Clim. Past Discuss.* **10**, 65–104 (2014).
58. Fischer, H., Siggaard-Andersen, M.-L., Ruth, U., Röthlisberger, R. & Wolff, E. Glacial/interglacial changes in mineral dust and sea-salt records in polar ice cores: sources, transport, and deposition. *Rev. Geophys.* **45**, RG1002 (2007).
59. de Vernal, A., Gersonde, R., Goosse, H., Seidenkrantz, M.-S. & Wolff, E. W. Sea ice in the paleoclimate system: the challenge of reconstructing sea ice from proxies—an introduction. *Quat. Sci. Rev.* **79**, 1–8 (2013).
60. Wolff, E. W. *et al.* Southern Ocean sea-ice extent, productivity and iron flux over the past eight glacial cycles. *Nature* **440**, 491–496 (2006).
61. Alley, R. *et al.* Changes in continental and sea-salt atmospheric loadings in central Greenland during the most recent deglaciation: model-based estimates. *J. Glaciol.* **41**, 503–514 (1995).
62. Noone, D. & Simmonds, I. Sea ice control of water isotope transport to Antarctica and implications for ice core interpretation. *J. Geophys. Res.* **109**, D07105 (2004).
63. Veres, D. *et al.* The Antarctic ice core chronology (AICC2012): an optimized multi-parameter and multi-site dating approach for the last 120 thousand years. *Clim. Past* **9**, 1733–1748 (2013).
64. Bazin, L. *et al.* An optimized multi-proxy, multi-site Antarctic ice and gas orbital chronology (AICC2012): 120–800 ka. *Clim. Past* **9**, 1715–1731 (2013).
65. Kawamura, K. *et al.* Northern Hemisphere forcing of climatic cycles in Antarctica over the past 360,000 years. *Nature* **448**, 912–916 (2007).
66. Schilt, A. *et al.* Atmospheric nitrous oxide during the last 140,000 years. *Earth Planet. Sci. Lett.* **300**, 33–43 (2010).
67. Köhler, P., Knorr, G., Buiron, D., Lourantou, A. & Chappellaz, J. Abrupt rise in atmospheric CO_2 at the onset of the Bolling/Allerød: in-situ ice core data versus true atmospheric signals. *Clim. Past* **7**, 473–486 (2011).
68. Rosen, J. L. *et al.* An ice core record of near-synchronous global climate changes at the Bolling transition. *Nature Geosci.* **7**, 459–463 (2014).
69. Köhler, P., Knorr, G. & Bard, E. Permafrost thawing as a possible source of abrupt carbon release at the onset of the Bolling/Allerød. *Nature Comm.* **5**, 5520 (2014).



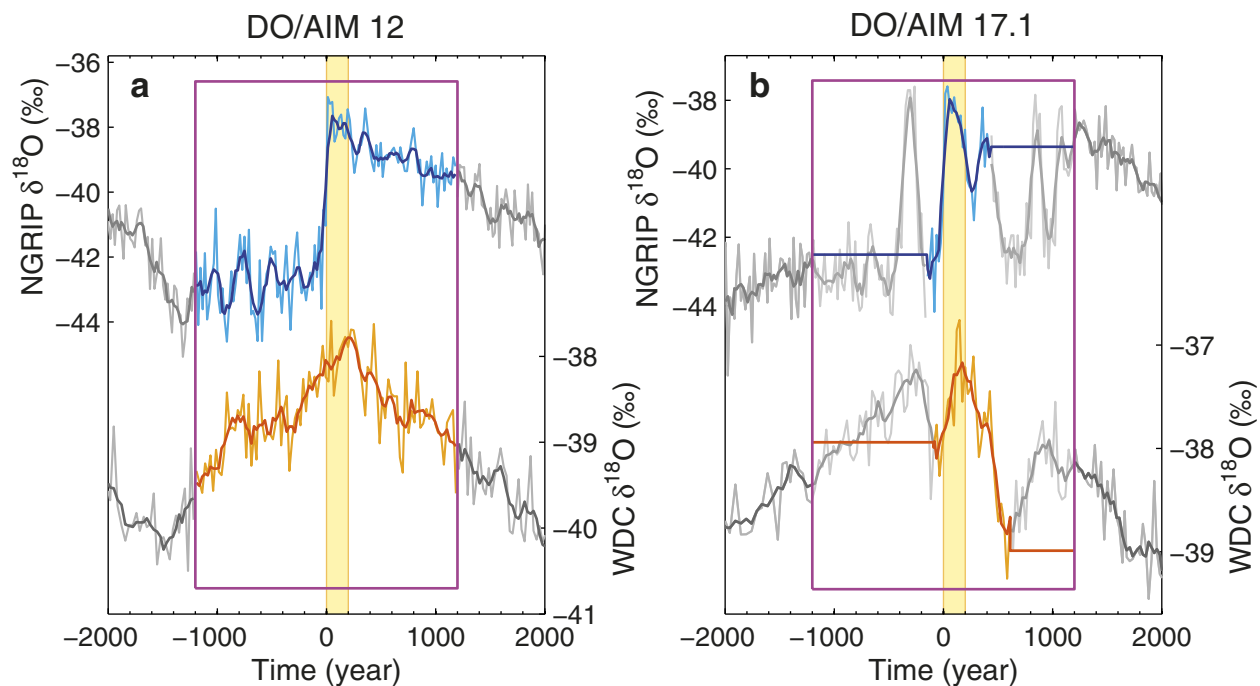
Extended Data Figure 1 | Difference between gas age and ice age (Δ age) at WAIS Divide. **a**, Comparison of WDC Δ age with other Antarctic cores. Ice core abbreviations: EDC, EPICA Dome Concordia; EDML, EPICA Dronning Maud Land; TALDICE, Talos Dome; WDC, WAIS Divide. Δ age values are taken from refs 23, 63–65. The vertical axis is on a logarithmic scale. **b**, Δ age uncertainty bounds obtained from an ensemble of 1,000 alternative Δ age

scenarios; details are given elsewhere²³. A Δ age scenario obtained with an alternative densification model (ref. 39 instead of ref. 38) is shown in blue. **c–e**, Histograms of the 1,000 Δ age scenarios at 20 kyr BP (**c**), 40 kyr BP (**d**) and 60 kyr BP (**e**); stated values give the distribution mean \pm the 2σ standard deviation.



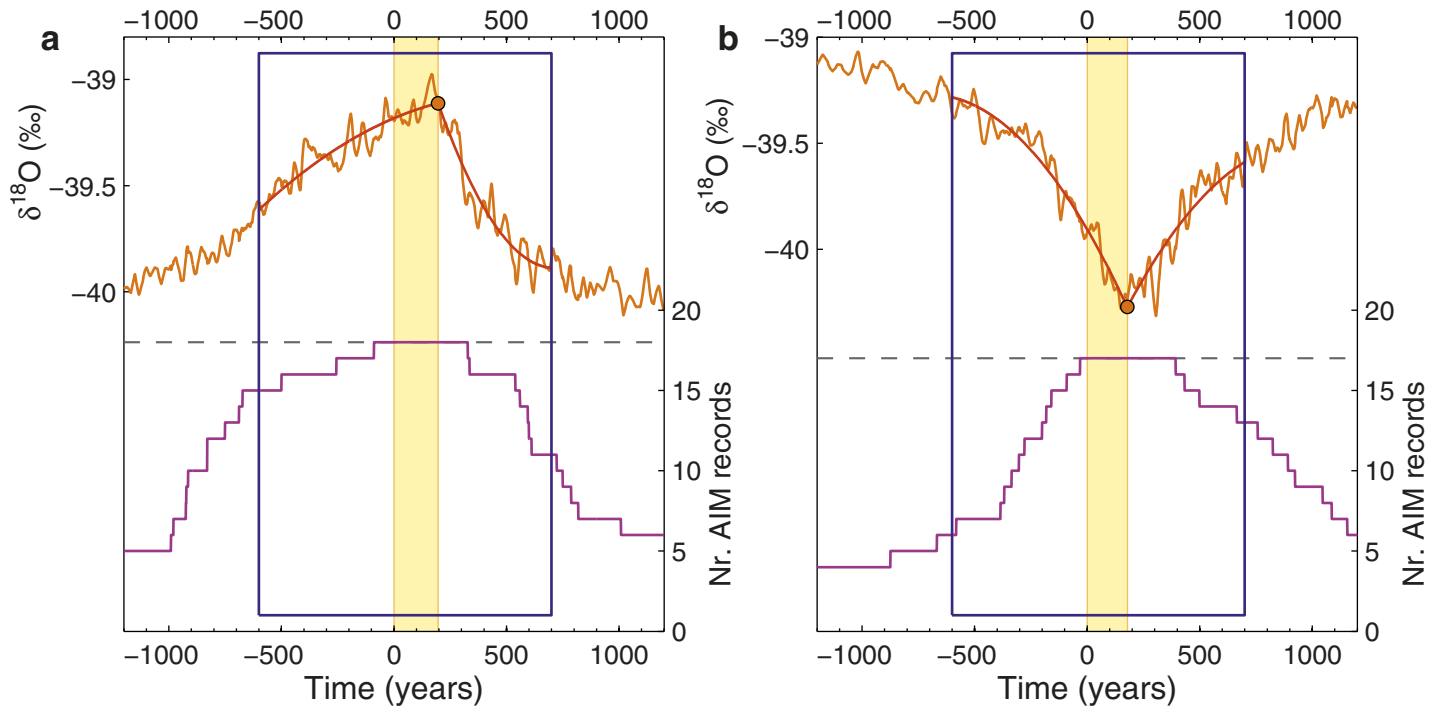
Extended Data Figure 2 | Determining the timing of the abrupt DO transitions. **a, b,** DO 17.2, 17.1, 16.2 and 16.1 (from oldest to youngest⁴¹) as recorded in NGRIP $\delta^{18}\text{O}$ (**a**) and WDC CH_4 (**b**). Horizontal orange bars denote pre-transition and post-transition levels; the transition midpoint (50% of signal amplitude) is indicated by a red dot; the 25% and 75% signal amplitude markers

are indicated with blue dots. **c,** Comparison of WDC CH_4 (grey) with EDML CH_4 (orange)^{3,50,66}. **d,** Hypothetical gas-age distribution for WDC due to firm densification and gradual bubble closure, using a truncated log-normal distribution⁶⁷. **e,** Shift in transition midpoint induced by filtering of the atmospheric record in the firm column.



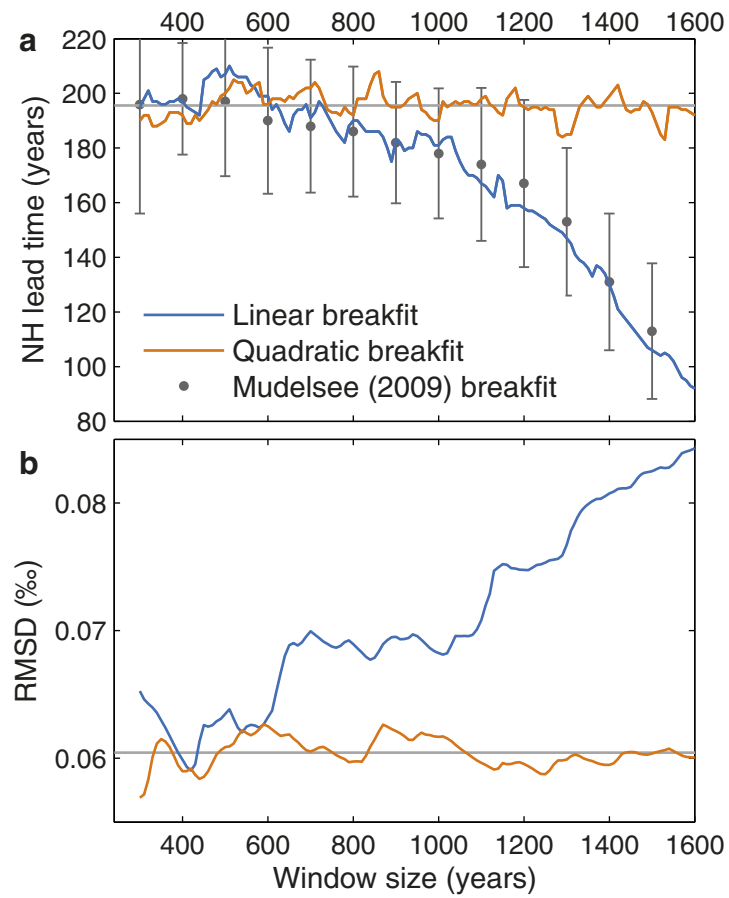
Extended Data Figure 3 | Cropping of individual records in the stack to prevent overlap of events. **a**, DO/AIM 12, where no cropping is needed. **b**, DO/AIM 17.1, where the most cropping is needed. Full time series with five-point running average are plotted in grey, and the contributory records are

plotted in blue and orange for NGRIP and WDC, respectively. The yellow vertical shading bar in background shows the NH lead time (200 years); the purple rectangle gives the $-1,200$ to $+1,200$ time window.



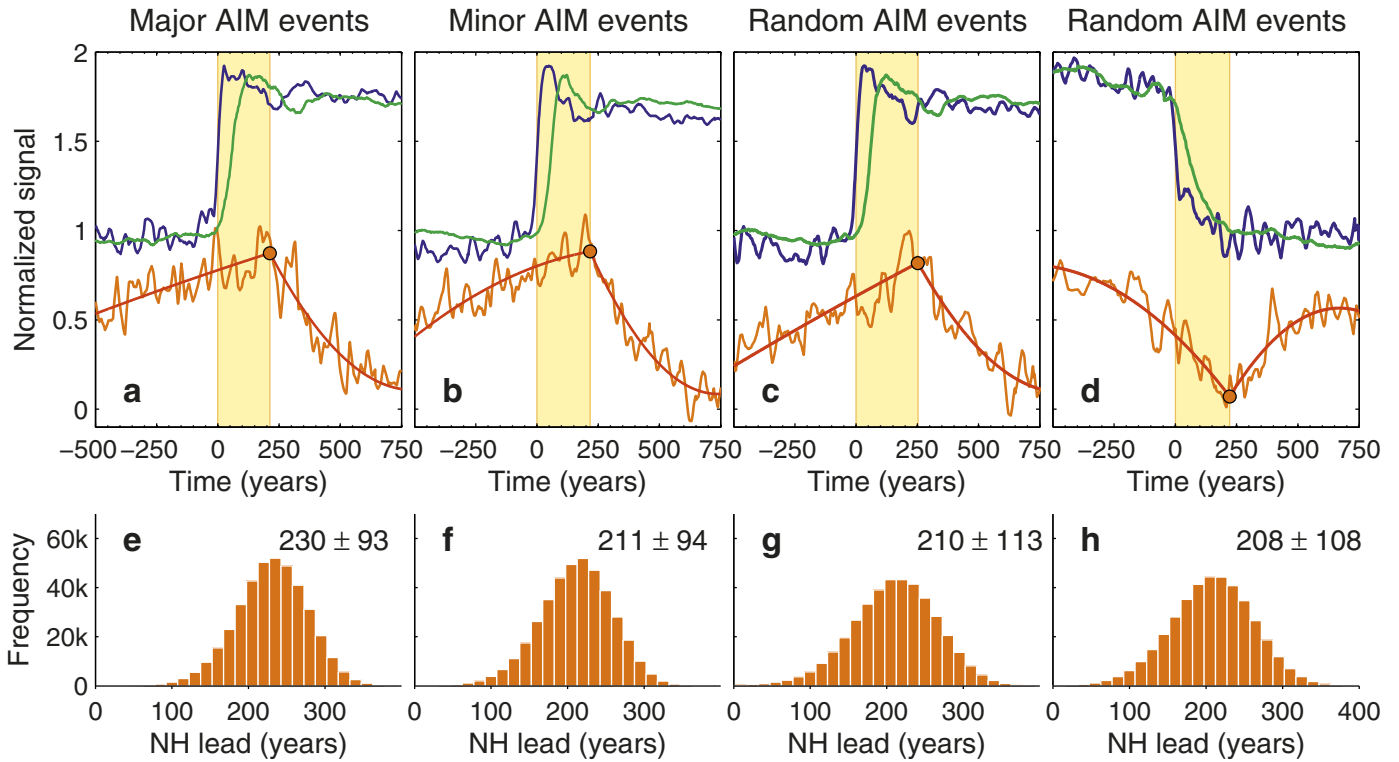
Extended Data Figure 4 | Number of records and fitting procedure. Number of contributory records to the WDC $\delta^{18}\text{O}$ stacks for abrupt NH warming (interstadial onset) (a) and for abrupt NH cooling (interstadial

termination) (b). Blue rectangles indicate the time window over which the fitting procedure evaluates the fit to the data (-600 to +700 years); shaded vertical yellow bars show NH lead time.



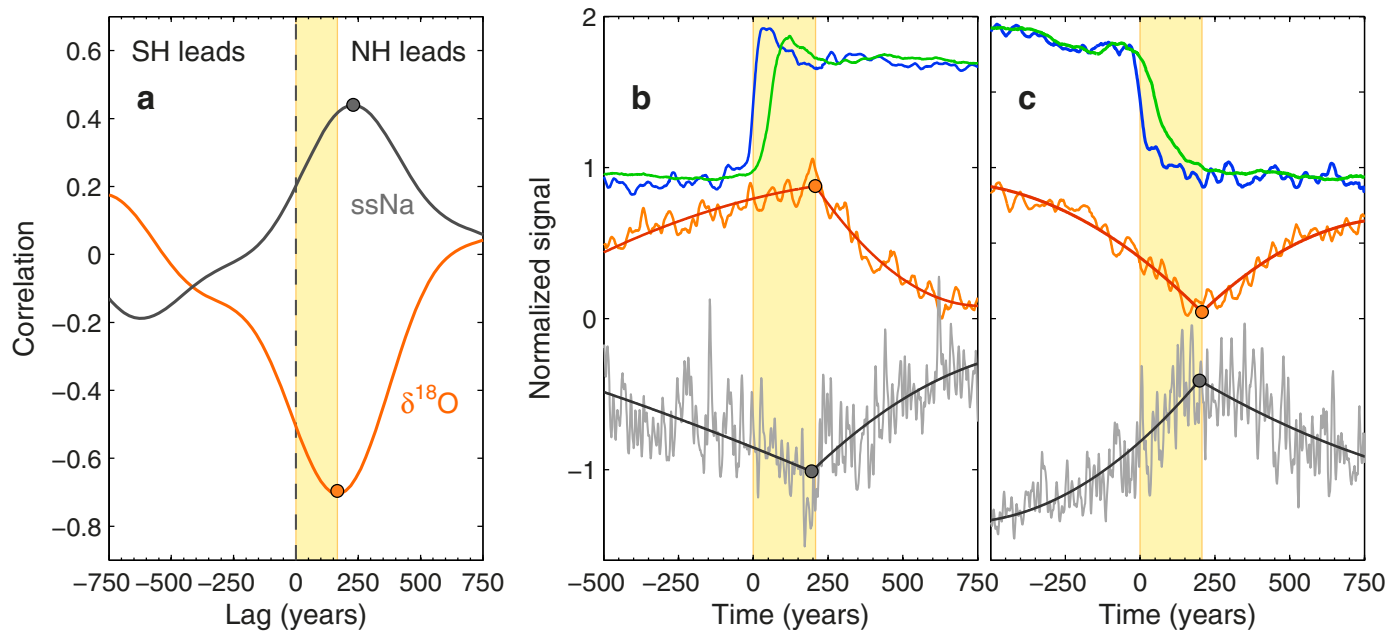
Extended Data Figure 5 | Evaluating the performance of the breakpoint detection algorithm. **a**, Breakpoint detection as a function of data window size using both linear (blue) and quadratic (orange) functions, compared with the BREAKFIT algorithm⁴⁸ (grey dots with 1σ error bars). The data window is

applied symmetrically, meaning that equal numbers of years (half the window size) are used before and after the detected breakpoint. Data falling outside this window are ignored in the fitting procedure. **b**, Root mean square deviation between the WDC $\delta^{18}\text{O}$ stack and the fitting curve.



Extended Data Figure 6 | Alternative stacking of AIM events. **a**, Stack of NGRIP $\delta^{18}\text{O}$ (blue), WDC CH_4 (green) and WDC $\delta^{18}\text{O}$ (orange with fit) for just the major AIM events (4, 8, 12, 14 and 17), aligned at the abrupt NH warming. **b**, As in **a**, but for only the minor AIM events (3, 5.1, 5.2, 6, 7, 9, 10, 11, 13, 15, 16 and 18). **c**, As in **a**, but for eight randomly selected DO/AIM events. **d**, As in **c**, but aligned at the abrupt NH cooling. Events are averaged with their

original amplitudes and normalized after stacking for convenience of visualization. **e–h**, Histograms of NH lead time associated with **a–d**, respectively, generated by binning the 4×10^5 solutions from the sensitivity study. The distribution mean and 2σ uncertainty bounds are listed in the panels. Shaded vertical yellow bars (upper panels) show NH lead time.



Extended Data Figure 7 | Timing of sea-salt sodium. **a**, Lagged correlation between NGRIP $\delta^{18}\text{O}$ and the time derivative of WDC $\delta^{18}\text{O}$ (orange), and between NGRIP $\delta^{18}\text{O}$ and the time derivative of WDC ssNa (grey). The dots indicate the maximum (anti-)correlation at 167-year and 229-year NH lead for WDC $\delta^{18}\text{O}$ and ssNa, respectively. A fourth-order Butterworth bandpass filter with a 500–10,000-year window is applied to the time series to isolate the millennial-scale variability. **b**, DO3–18 stack of NGRIP $\delta^{18}\text{O}$ (blue), WDC CH_4

(green), WDC $\delta^{18}\text{O}$ (orange) and WDC ssNa (grey), aligned at the midpoint of the DO warming signal. The estimated breakpoint in the stacks (dots) occurs at $t = 218$ and 195 years for WDC $\delta^{18}\text{O}$ and ssNa, respectively. **c**, As in **b**, but for the abrupt NH cooling events, with the estimated breakpoint at $t = 208$ and 199 years for WDC $\delta^{18}\text{O}$ and ssNa, respectively. Shaded vertical yellow bars show NH lead times.

Extended Data Table 1 | Phasing of the bipolar seesaw during the last deglaciation

Transition	WDC $\delta^{18}\text{O}$ breakpoint	WDC CH_4 Transition	Δage	Greenland – CH_4 phasing	Lead of NH climate
OD – B/A	$14,350 \pm 110$	$14,576 \pm 29$	228 ± 62	30 ± 32	256 ± 133
B/A – YD	$12,778 \pm 80$	$12,764 \pm 53$	218 ± 68	30 ± 32	16 ± 122
		$12,881 \pm 30^\dagger$	216 ± 67	30 ± 32	$133 \pm 113^\dagger$
YD – Holoc.	$11,842 \pm 90^\ddagger$	$11,542 \pm 33$	195 ± 52	30 ± 32	$-270 \pm 114^\ddagger$

For the deglaciation we use a Greenland- CH_4 phasing that is the average of the 56 ± 38 -year CH_4 lag observed for the glacial period^{24,46}, and the near-synchronous phasing (4.5 ± 24 -year CH_4 lag) observed for the Bølling transition⁶⁸. All stated errors represent 2σ uncertainty bounds; uncertainty in the WDC $\delta^{18}\text{O}$ breakpoint is determined using the BREAKFIT algorithm⁴⁸; uncertainty in the CH_4 transition is defined as the 25–75% range of the CH_4 transition (Extended Data Fig. 2); Δage uncertainty is found by using a firn densification model sensitivity study²³ (Extended Data Fig. 1); uncertainty in the Greenland- CH_4 phasing is taken to be the root mean square of the uncertainties in the cited studies^{24,68}; the uncertainty in the NH climate is the root sum square of the uncertainties in the preceding columns. The potential role of CO_2 in delaying Antarctic cooling at the Bølling onset is discussed in ref. 69.

[†] This estimate uses the onset, rather than the midpoint, of the Bølling–Allerød to Younger Dryas transition in WDC CH_4 in determining the phasing.

[‡] This estimate may be unreliable because of a double peak in WDC $\delta^{18}\text{O}$ at about this time that may reflect local climate, as well as a unique and pronounced accumulation anomaly starting at about 11.9 kyr BP.